Journal Name

ARTICLE TYPE

Cite this: DOI: 00.0000/xxxxxxxxxx

Supplementary materials for article "Direct observation of split-mode exciton-polaritons in a single MoS_2 nanotube"

A.I. Galimov[a], D.R. Kazanov[a], A.V. Poshakinskiy[a], M.V. Rakhlin[a], I.A. Eliseyev[a], A.A. Toropov[a], M. Remškar[b] and T.V. Shubina*[a]

Received Date
Accepted Date

DOI: 00.0000/xxxxxxxxxx

An optical double-well potential

There is an analogy between a double-well potential for a particle and that for the electric field in a NT with a flattened cross-section (Fig. S1). If the thickness of the barrier between the two potential wells b is very large, the particles can reside in the left or right well, and the eigenstates are twice degenerate. When the thickness of the barrier is decreased, the tunneling between the wells arises and mixes the wave functions of the particle states. Then, the eigenstates are the even and odd superposition of the states in the two wells, i.e. $\Psi_{e,o} = \frac{1}{\sqrt{2}}(\psi_1 \mp \psi_2)$ and the corresponding eigenenergies are equal to $E_{e,o} = E_0(1 \pm t)$. The magnitude of the splitting is determined by the exponential factor $t \propto e^{-\kappa b}$, where κ is the imaginary part of the wave vector of the particle in the barrier, which grows rapidly as the wells move closer to each other.

A similar phenomenon occurs with electromagnetic field in a NT. In the non-deformed NT, the field is strongly confined inside the wall and the tunneling is negligible. The eigenstates, characterized by their azimuthal number m, can propagate clockwise or counterclockwise. Thus, they are twice-degenerate, since their frequency $\omega_m \sim mc/(2n_{\text{eff}}r)$ depends only on m and NT radius r. Here c is the speed of light and n_{eff} is the effective refractive index of the mode, which is some average between the refractive index of the NT material and air.

As we squeeze the NT cross-section, the gap between the longer parts decreases and the evanescent tails begin to overlap. Now the eigenstates represent the standing waves, even and odd with respect to the major axis of the cross-section. The energy of the split modes are $\hbar\omega_{e,o} = \hbar\omega_0(1 \mp t_{\text{WGM}})$. With further deformation of the cross-section, the splitting increases exponentially $t_{\text{WGM}} \propto e^{-\kappa_r b}$, where b is the minor axis of the NT cross-section and $\kappa_r = \omega/c\sqrt{n_{\text{eff}}^2 - 1}$ is the decay rate of the evanescent tail outside the NT wall. In the limit of a fully collapsed NT, the system reduces to a conventional Fabri-Pérot resonator.

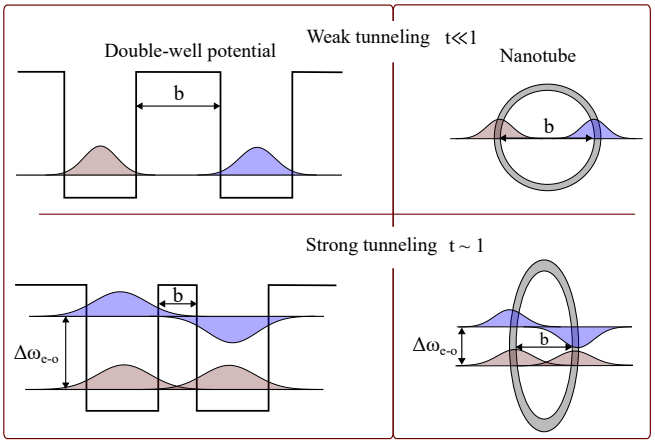

Fig. S1 An analogy between a particle in a double-well potential and an optical mode in a NT wall. (Upper part) No tunneling with thick barrier (gap), wave functions (electric fields) do not overlap, degenerate eigenenergies. (Lower part) Strong tunneling with thin barrier (gap), eigenstates are mixed, and the eigenenergies are split

NT shape characterization

To determine the tube shape, we carried out optical measurements using a microscope in the Horiba LabRam HR Evolution spectrometer. The microscope is equipped with a precision XY stage SCANPlus and a motorized focus drive MA-42 (Märzhäuser, Wetzlar, Germany), which allowed us to control the focusing distance (Z coordinate) and the position in the substrate plane (X and Y coordinates) with high accuracy ($\sim$ 20 nm).

* Email: shubina@beam.ioffe.ru
[a] Ioffe Institute, 26 Politekhnicheskaya, St. Petersburg, 194021, Russia.
[b] Jozef Stefan Institute, 39 Jamova cesta, Ljubljana, 1000, Slovenia.

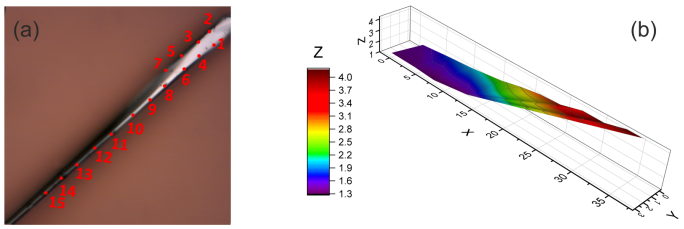

Fig. S2 (a) Bright-field image of the studied NT. The numbers indicate points where the NT height was measured. (b) Measured NT profile. Distances and height are given in micrometers. $(X,Y)=(0,0)$ corresponds to point No. 1 in (a).

The focal point and, therefore, the Z coordinate was determined by the maximum reflection when illuminated with white light. In Fig. S2 (b) shows the shape and dimensions of the tube obtained from the 15 points marked in Fig. S2 (a). Here, the zero point in the Z direction corresponds to the substrate plane. From this experiment we can estimate that the radius of the undeformed equivalent tube is $\sim 800-1000$ nm, the aspect ratio of the tube at points No. 1, 2 is about 1:3, and at point No. 15 it is about 1:10.

Raman measurements

First, it is worth noting that the effects of deformation differ in single-walled and multi-walled NTs. All experimental samples are multi-walled, and single-walled NTs are realized very rarely[1], but are a favorite object of theoretical research.[2–5]. In single-walled NTs, the tensile strain due to surface curvature is significant at small diameters, but as the diameter increases, the strain decreases because the flatter the surface, the smaller the stretching of atomic bonds. As shown by Seifert et al.[2,6], this is accompanied by an increase in the band gap energy (blue shift) up to the planar monolayer limit. A different situation is realized in multi-walled NTs, when each subsequent monolayer must maintain the stacking order with respect to the previous layers, stretching over them. The resulting tensile strain reduces the band gap[7], similar to what is observed in atomically-thin layers with tension[8]. In additon, the energy gap between excitons A and B may deviate from its value in unstrained material due to the difference in the change in their energies upon deformation[9].

To show that the studied NT undergoes tensile deformation, we performed combined micro-Raman and micro-PL studies. When comparing the Raman spectrum of a NT with the spectrum of freshly exfoliated bulk MoS_2 (Fig. S3), we observe a significant redshift of both E_{2g} and A_{1g} lines. In general, the redshift of Raman lines indicates the presence of tensile strain, which is expected to be uniaxial in the tubes. Quantitative estimation of the magnitude of strain in a multiwall NT based on the Raman data is a complex task. According to the data of several existing works on uniaxially strained multilayer MoS_2 [10,11], such a shift may point to the strain values from $\sim(1.5-2)\%$[10] to $\sim(3-8)\%$[11]. According to the strain-induced direct band gap shift obtained in[10], the observed A-exciton shift of more than one hundred meV may indicate $\sim 6\%$ tensile strain. However, these estimates are qualitative in nature, since the deformation in the NT is very specific

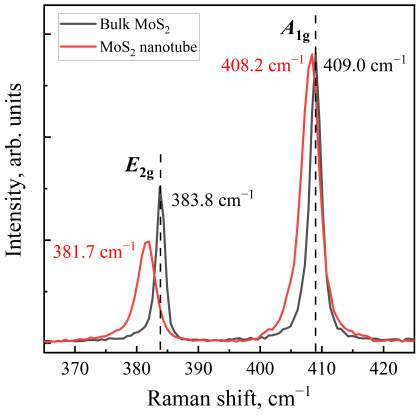

Fig. S3 Raman spectra of the NT and a bulk MoS_2 crystal. Dashed lines demonstrate the positions of E_{2g} and A_{1g} lines of bulk MoS_2. Frequencies of the E_{2g} and A_{1g} lines are indicated for each of the lines in the corresponding color.

and possible 3R stacking in the NT layers may contribute to this shift. Only the tensile strain $\geq 1\%$ can be reliably indicated, which justifies the red shift of the exciton resonances.

Model of reflection from a flattened NT

Let the plane wave $E_{\rm inc}=e^{\mathbf{ikr}}$ polarized along the NT axis fall on the NT in normal incidence at angle α with the minor axis. The matrix element $t_{\rm in}^{(m)}$ of excitation of an even or odd WGM $E_m^{(\rm e,o)}$ is determined by the overlap integral,

$$t_{\rm in}^{(m)}=\int E_m^{(\rm e,o)}E_{\rm inc}\,d\varphi \tag{1}$$

as in[12]. Accordingly, the electric field amplitude inside the NT is expressed as

$$A_{\rm mode}^{(m)}=\frac{t_{\rm in}^{(m)}}{\omega-\omega_{\rm e,o}^{(m)}(b)+{\rm i}(\Gamma+\Gamma_0)}, \tag{2}$$

where $\omega_{\rm e,o}^{(m)}(b)\approx\omega_0^{(m)}(1\mp Ce^{-(\omega/c)b\sqrt{n_{\rm eff}^2-1}})$ is the dispersion of even/odd WGMs with angular number m, Γ,Γ_0 are homogeneous and inhomogeneous broadening of WGMs, respectively.

This is followed by the reverse process of light emission from the NT. The efficiency of the scattering process is also determined by the overlap of the WGM electric field and the scattered electric field

$$t_{\rm out}^{*(m)}=\int E_m^{(\rm e,o)}E_{\rm scatt}^{*}\,d\varphi, \tag{3}$$

so the scattered field amplitude reads

$$A_{\rm scat}^{(m)}=A_{\rm mode}^{(m)}t_{\rm out}^{*(m)}. \tag{4}$$

Thus, full reflection R would be a sum of all modes that interact with the incident field

$$R(\omega,b)\propto\left|\sum_m A_{\rm scat}^{(m)}\right|^2=\left|\sum_m\frac{t_{\rm out}^{*(m)}t_{\rm in}^{(m)}}{\omega-\omega_0^{(m)}(1\mp Ce^{-(\omega/c)b\sqrt{n_{\rm eff}^2-1}})+{\rm i}(\Gamma+\Gamma_0)}\right|^2. \tag{5}$$

For weakly deformed NTs, the matrix element of the WGM excitation can be found as a convolution of the WGM electric field $E_{\text{mode}} = E_0 \sin(m\varphi)$ or $E_0 \cos(m\varphi)$ with incident electric field in a form of a plane wave $E_{\text{inc}} = \tilde{E}_0 e^{ik_z r \sin(\varphi-\alpha)}$ propagating in the direction determined by the angle α. Following the decomposition of a plane wave in cylindrical waves $e^{iz\sin\varphi} = \sum_{n=-\infty}^{\infty} J_n(z) e^{in\varphi}$ we express the coupling efficiency, for example, for odd mode as

$$t_{\text{in}}^{(m)} = \int E_{\text{m}}^{(e)} E_{\text{inc}} d\varphi = \int E_0 \sin(m\varphi) \tilde{E}_0 e^{ik_z r sin(\varphi-\alpha)} d\varphi = \quad (6)$$

$$\sum_{n=-\infty}^{+\infty} E_0 \tilde{E}_0 J_n(k_z r) \int \sin(m\varphi) e^{in(\varphi-\alpha)} d\varphi. \quad (7)$$

Using properties of trigonometric functions one could obtain coupling efficiency for odd and even mode, respectively

$$t_{\text{in}}^{(o,m)} = 2\sqrt{2}\pi E_0 \tilde{E}_0 e^{i\frac{\pi}{4}(2m-1)} J_m(k_z r) \sin(m[\alpha + \frac{\pi}{2}]) \quad (8)$$

$$t_{\text{in}}^{(e,m)} = 2\sqrt{2}\pi E_0 \tilde{E}_0 e^{i\frac{\pi}{4}(2m-1)} J_m(k_z r) \cos(m[\alpha + \frac{\pi}{2}]). \quad (9)$$

Determination of optical parameters

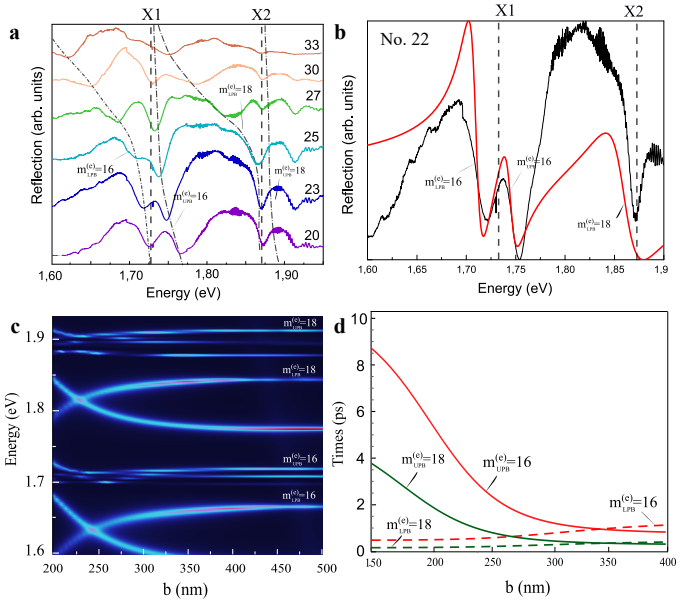

Fig. S4 (a) Raw reflection spectra selected among the region of points 20—33 of Fig. 2 from main text. Thin lines show upper and lower polariton branches of two optical modes with $m = 16, 18$. (b) Experimental reflection spectra (black line) corresponding to the point 22 and its fit (red line) by eq. (5) for several WGMs near A- and B-exciton resonances. (c) Calculated optical modes for studied NT depending on the degree of flattening. (d) Decay times of two optical modes with $m = 16, 18$ for UPB and LPB. Solid line and dashed line are UPB and LPB for modes $m = 16, 18$, respectfully.

Figure S4 illustrates the process of determining the optical parameters of NT. The raw reflectance spectra are shown in Fig. S4 (a). We will focus on two modes close to exciton resonances with angular numbers $m = 16$ and $m = 18$. The dispersion of WGM polaritons is shown by thin dash-dot lines. To obtain WGM mode energies near exciton resonances, we fit the experimental spectra with analytical model for reflection Eq. (5) (red line in Fig. S4 (b). The decay time obtained from the analytical approximation is about $0.2-0.5$ ps for both modes. To quantitatively describe the dynamics of hybrid exciton-polariton states, we used the results of numerical calculations of flattened WGMs obtained by solving Maxwell's equations Fig. S4 (c). We took idealized decay times of 10 ps and 5 ps for excitons A and B, respectively. The inverse imaginary part of the solutions expresses the decay times of UPB and LPB polaritons with different degrees of flattening of the NT cross-section (Fig. S4 (d)). The highly flattened tube ($b = 150$ nm) exhibits a pure optical mode regime for LPB (dashed lines) with a decay time similar to that of a pure WGM. And UPBs (solid lines) have decay times of almost pure excitons. Another case is a weakly flattened NT ($b > 350$ nm), where we observe a decrease in decay times for both UPB and LPB, indicating the proximity and interaction of optical modes and exciton resonances.

Time-resolved photoluminescence measurements

To elucidate the dynamics of polariton, we performed time-resolved photoluminescence (TRPL) measurements on all PL peaks in the spectrum in Fig. 4 (b) in the main text, as described in the Method section. The PL decay curves presented in Fig. S5 were modeled as

$$I_{\text{PL}}(t) = A_0 + A_1(e^{-t/t_1} - e^{-t/t_r}) + A_2 e^{-t/t_2} + A_3 e^{-t/t_3}, \quad (10)$$

where A_0 is the background amplitude. The ascending term with time constant $t_r \approx t_1 \sim 0.02$ ns has the same amplitude A_1 as the descending term t_1. Note that the time t_1 is determined by the accuracy of our setup, the real time can be somewhat smaller. Together, these terms model the sharp peak arising immediately after excitation (see Fig. 4 (e) of the main text, where an ascending term is added to all components for clarity). This fast component reflects the dynamics of photon part of the exciton-polariton, while the exciton part is given by the second term with the characteristic decay time which varies from 230 ps to 90 ps as the peak wavelength decrease. The slowest component with the decay time varied from 1.2 to 0.4 ns with the wavelength decrease is associated with the emission of indirect exciton arising from modification of the band structure under tensile strain. Us-

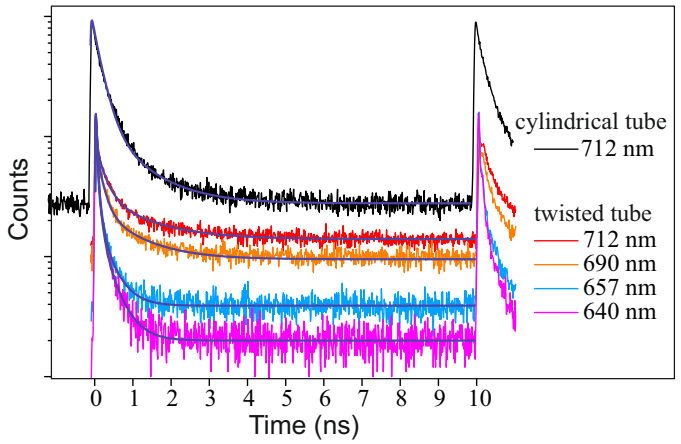

Fig. S5 PL decay curves measured in the twisted and cylindrical tubes.

ing these fits, we can calculate the ratio of i-contribution to their sum: $A_i t_i / \sum A_i t_i$. For the PL peak at 712 nm (LPB in Fig. 4 (e)), we found at least a 30-fold increase in this photonic contribution in the twisted tubes compared with the cylindrical tube. An additional two-fold enhancement of this component occurs at the B exciton resonance, which has a higher oscillator strength.

Notes and references

1 M. Remškar, A. Mrzel, Z. Skraba, A. Jesih, M. Ceh, J. Demšar, P. Stadelmann, F. Lévy and D. Mihailovic, *Science*, 2001, **292**, 479–481.

2 G. Seifert, H. Terrones, M. Terrones, G. Jungnickel and T. Frauenheim, *Phys. Rev. Lett.*, 2000, **85**, 146–149.

3 N. Zibouche, A. Kuc and T. Heine, *Eur. Phys. J. B*, 2012, **85**, 49.

4 H.-H. Wu, Q. Meng, H. Huang, C. T. Liu and X.-L. Wang, *Phys. Chem. Chem. Phys.*, 2018, **20**, 3608–3613.

5 K. Hisama, M. Maruyama, S. Chiashi, S. Maruyama and S. Okada, *Jpn. J. Appl. Phys.*, 2021, **60**, 065002.

6 G. Seifert, H. Terrones, M. Terrones, G. Jungnickel and T. Frauenheim, *Solid State Commun.*, 2000, **114**, 245–248.

7 M. Ghorbani-Asl, N. Zibouche, M. Wahiduzzaman, A. F. Oliveira, A. Kuc and T. Heine, *Sci. Rep.*, 2013, **3**, 2961.

8 H. J. Conley, B. Wang, J. I. Ziegler, R. F. Haglund Jr., S. T. Pantelides and K. I. Bolotin, *Nano Lett.*, 2013, **13**, 3626–3630.

9 D. Lloyd, X. Liu, J. W. Christopher, L. Cantley, A. Wadehra, B. L. Kim, B. B. Goldberg, A. K. Swan and J. S. Bunch, *Nano Lett.*, 2016, **16**, 5836–5841.

10 L. Yang, X. Cui, J. Zhang, K. Wang, M. Shen, S. Zeng, S. A. Dayeh, L. Feng and B. Xiang, *Sci. Rep.*, 2014, **4**, 5649.

11 C. K. Tan, W. C. Wong, S. M. Ng, H. F. Wong, C. W. Leung and C. L. Mak, *Vacuum*, 2018, **153**, 274–276.

12 I. A. Eliseyev, B. R. Borodin, D. R. Kazanov, A. V. Poshakinskiy, M. Remškar, S. I. Pavlov, L. V. Kotova, P. A. Alekseev, A. V. Platonov, V. Y. Davydov and T. V. Shubina, *Adv. Opt. Mater.*, 2023, 2202782.